Microchimica Acta (2020) 187:553
https://doi.org/10.1007/s00604-020-04490-6

ORIGINAL PAPER

# Hierarchical multifunctional graphene oxide cancer nanotheranostics agent for synchronous switchable fluorescence imaging and chemical therapy

Yasaman Esmaeili[1,2] · Ali Zarrabi[1,3,4] · Seyede Zohreh Mirahmadi-Zare[2] · Elham Bidram[5]

Received: 20 May 2020 / Accepted: 17 August 2020


## Abstract

A nanotheranostics platform was synthesized based on PEGylated graphene oxide–gold nanoparticles and specified with aptamer toward the MUC-1-positive tumor cells. Subsequently, it was loaded with doxorubicin, used for non-invasive fluorescence imaging and therapy of breast and colon tumors. The success of the nano-coating at each synthesis step was characterized through FTIR, XRD, TGA, FE-SEM, EDAX, Zeta-potential, and fluorescence spectroscopy. Besides, the ability of the designed platform in targeted imaging, drug delivery, and in vitro therapy were evaluated using fluorescence microscopy and flow cytometry. The selected aptamer acts as a quencher, resulting in an "on/off" fluorescence biosensor. When the aptamer specifically binds to the MUC-1 receptor, its double strands separate, leading to the drug release and the recovery of the fluorescence of ("On" state) at the excitation wavelength of 300 nm. Based on cell toxicity results, this platform has more toxicity toward the MUC-1-positive tumor cells (HT-29 and MCF-7) compared to MUC-1-negative cells (Hep-G2), representing its selective performance. Thus, this nano-platform can be introduced as a multifunctional cancer nanotheranostics system for tracing particular biomarkers, non-invasive imaging, and targeted chemotherapy.

**Keywords** Graphene oxide · Aptamer · Cancer nanotheranostics · Non-invasive imaging · Targeted therapy

**Highlights**
- *GO@PEG/Au/Apt/DOX as a new type of smart theranostic agent was fabricated.*
- *This new nanosystem has an "on/off" fluorescence biosensing ability.*
- *It also has selective performance against MUC-1-positive tumor cells.*
- *It is a nanotheranostics system for tracing particular biomarkers, non-invasive imaging, and targeted chemotherapy.*

**Electronic supplementary material** The online version of this article (https://doi.org/10.1007/s00604-020-04490-6) contains supplementary material, which is available to authorized users.

✉ Ali Zarrabi
alizarrabi@sabanciuniv.edu

✉ Seyede Zohreh Mirahmadi-Zare
mirahmadi_zare@royaninstitute.org

[1] Department of Biotechnology, Faculty of Biological Science & Technology, University of Isfahan, Isfahan, Iran

[2] Department of Animal Biotechnology, Reproductive Biomedicine Research Center, Royan Institute for Biotechnology, ACECR, Isfahan, Iran

[3] Sabanci University Nanotechnology Research and Application Center (SUNUM), Tuzla, 34956 Istanbul, Turkey

[4] Center of Excellence for Functional Surfaces and Interfaces (EFSUN), Faculty of Engineering and Natural Sciences, Sabanci University, Tuzla, 34956 Istanbul, Turkey

[5] Biosensor Research Center (BRC), Department of Biomaterials, Nanotechnology, and Tissue Engineering, School of Advanced Technologies in Medicine, Isfahan University of Medical Sciences (IUMS), Isfahan, Iran

Published online: 09 September 2020

## Introduction

Recent advances in nanotechnology have led to development of effective drug delivery systems for simultaneous early diagnosis and treatment of cancer, known as cancer theranostics [1–3]. A good nanotheranostics system utilizing tumor biomarkers [4] would be highly desirable for achieving both non-invasive diagnosis and targeted therapy [5, 6]. The identification of biomarker molecules, including nucleic acids, proteins, and small molecules associated with cancer that generally exist in human tissues and fluids (urine, blood, saliva, and cerebrospinal fluids) [7], play a key role in cancer diagnosis at early stages. Aptamers, as the single-stranded oligonucleotides with the designed structures, can selectively interact with specific biomarkers [8], such as Mucin 1 (MUC-1), a large trans-membrane glycoprotein, presented in a variety of malignant tumors [9]. Due to its unique properties including high stability, reproducibility, adaptability, ease of modification, and reduced immunogenicity and toxicity, aptamers offer an advantage over other targeting molecules [10].

Currently, non-invasive fluorescence imaging technology for molecular biomarker imaging has dramatically progressed [11]. Fluorescence imaging probes with the intense emission at far-red/near-infrared (FR/NIR) region (> 650 nm) are more attractive due to their capability of overcoming the interferences of optical absorption, light scattering, and autofluorescence of endogenous substances such as hemoglobin, cytochromes, and water molecules [12, 13]. Near-infrared fluorescence (NIRF) imaging detects the fluorescence emissions at 650–900 nm region, with the lower background (tissue) absorption for deeper penetration, thus making it suitable for preclinical and clinical imaging studies [14, 15]. To date, a large variety of materials, including organic dyes [16, 17], fluorescent proteins [18, 19], and inorganic nanomaterials [20] such as quantum dot (QD) [21, 22], have been widely studied for fluorescence imaging. However, organic dyes and fluorescent proteins have limited applications due to their molar absorptivity and low photobleaching thresholds [18]. Inorganic QDs, on the other hand, are highly cytotoxic, limiting the scope of their biomedical applications [22]. Thus, the discovery of a novel fluorescence probe with a high biological compatibility, strong photobleaching resistance, and efficient light emission is highly desirable for non-invasive imaging [23]. Graphene oxide (GO) and gold nanoparticles (AuNPs) have recently emerged as the autofluorescence materials for non-invasive bio-imaging and targeted therapy [24] due to their unique advantages such as synthetic versatility, low cytotoxicity, high photostability, tunable optical properties, brightly emissive for high-contrast imaging, and facile surface functionalization for specific targeting [25]. GO, a two-dimensional sp2-hybridized carbon sheet with exceptional electrical, mechanical, thermal, and chemical properties have widely been attracted for biomedical applications, including drug/gene delivery carriers [26–28], biosensors [29, 30], and bio-imaging probes [31, 32]. The quenching of GO fluorescence by fluorophores, such as QD and AuNPs [33, 34], and the quenching effect of GO on some fluorescence molecules have both been reported [35–37]. In fact, the dual roles of GO as a fluorophore and a quencher at the same time make it attractive and highly promising for biosensor design. GO with the typical C/O ratio (2:4) tolerates the widespread fluorescence from visible to near infrared (NIR) range, with the maximum intensity located in the 500–800 nm range [38, 39]. Bidram et al. in 2016 showed the ability of GO derivatives to emit in three fluorescence regions (blue, green, and red) for the first time [40]. To increase the time circulation of GO in the biological environment, low molecular weight polyethylene glycol (PEG) has been attached to the GO, reducing the steric hindrance between the targeting ligand and biomarker, and increasing the hydrophilicity of the modified polymeric networks [41]. PEG has the ability to hide the conjugation from reticulo-endothelial system (RES) evading their uptake by macrophages and reducing the overall systemic toxicity [42].

AuNPs are very attractive due to their ultrafine size, large Stokes shift, good biocompatibility, their capacity for binding to biomolecules through Au–sulfur bonds, and light-scattering properties [43]. The localized surface plasmon resonance (LSPR) of AuNPs enables their development as a promising bio-imaging probe in biomedical applications [44]. The plasmonic properties of AuNPs provide us with the opportunity to record high-resolution imaging, overcoming the diffraction limit [45, 46]. Furthermore, they increase the excitation of fluorescence probes, enabling deep tissue imaging by enhancement of two/multi-photon absorption [43].

In the present study, GO@PEG/Au platform was fabricated layer by layer, potentially applicable for non-invasive imaging based on autofluorescence. In order to target specific tumor cells overexpressing MUC-1, a particular aptamer was coupled to the gold nanoparticles and doxorubicin (DOX) as the common anticancer agent was then loaded onto the obtained system. GO@PEG/Au/Apt (DOX) multifunctional cancer nanotheranostics conjugate is introduced for a dual non-invasive fluorescence imaging/targeted therapy.

## Materials and methods

### Materials

GO, 1-ethyl-3-(3-dimethylaminopropyl) carbodiimide (EDC), and chloroauric acid ($HAuCl_4$) were purchased from Sigma, USA; polyethylene glycol (PEG6000) was purchased from ROTH, Germany; and 4-dimethylaminopyridine (DMAP), dimethyl sulfoxide (DMSO), sodium citrate, and DOX were

purchased from Merck, Germany. 1,4-Dithiothreitol (DTT) was purchased from Bio-Rad, Iran. Dulbecco's modified Eagle medium (DMEM), penicillin/streptomycin (pen/strep), L-glutamine, non-essential amino acid (NEAA), and trypsin-EDTA enzyme were purchased from Gibco, USA. 3-(4, 5-Dimethylthiazol-2-yl)-2, 5-diphenyltetrazolium bromide (MTT) and fetal bovine serum (FBS) were purchased from Sigma, USA. Aptamer (5′-GCCCGCCGTGGCTGGGTCTT CCTTGGT CGGTCTACAAAAAAAAAA-SH-3′) was ordered from SBS Genetech Co. Ltd. MCF-7 (breast cancer cell line), HT-29 (colon cancer cell line), and HepG-2 (liver cancer cell line) were purchased from Pasteur Institute of Iran.

## Characterization

The physico-chemical properties of the obtained nano-system in each step were characterized using Fourier-transform infrared spectroscopy (FTIR; JACSO 6300, Japan), X-ray diffraction (XRD; Asenware AW-DX300, Germany), scanning electron microscopy (SEM; TESCAN MIR3, Czech Republic), and fluorescence spectrometer (PerkinElmer, LS 55). In addition, zeta potential measurements were performed using a Malvern Zeta instrument to investigate the charge surface of nano-system. Inductively coupled plasma optical emission spectrometry (ICP-OES; Varian-735-ES, Australia) was used to determine the concentration of chemical elements, especially gold.

## Methods

### Synthesis of GO@PEG/Au/Apt platform

To prepare PEGylated graphene oxide, EDC and DMAP were used to covalently bond PEG onto the GO surface via ester bond formation [47]. Afterwards, AuNPs were synthesized separately using Turkevich method based on reduction of the $HAuCl_4$ by citrate in water [48]. Then, the synthesized AuNPs were added to the GO@PEG solution under sonication. The synthesis of the final GO@PEG/Au/Apt conjugate was performed according to our previous study [49], in which the thiol (–SH) group at the end of aptamer was first activated with DTT solution and then the activated aptamer was mixed with GO@PEG/Au solution and linked to the AuNPs via covalent bond. The details of synthesis of each conjugate are described in the electronic supplementary information (ESI).

### Loading DOX into the GO@PEG/Au/Apt

DOX was dissolved in phosphate buffer (pH 7.4) and then was mixed with GO@PEG/Au/Apt aqueous dispersion (with the weight ratio of 1:1; nano-system—DOX) while vigorously shaken for 24 h. To quantify free DOX, standard curve was prepared by measuring the UV absorbance of a series of DOX solutions at 488 nm with the known concentrations in phosphate buffer. The DOX loading capacity and the entrapment efficiency were calculated based on the following Eqs. 1 and 2:

$$\%\text{Loading capacity (LC)} = \frac{\text{Total DOX added (wt)} - \text{DOX unentrapped (wt)}}{\text{Total nanocarrier (wt)}} \times 100 \quad (1)$$

$$\%\text{Entrapment efficiency (EE)} = \frac{\text{Total DOX added (wt)} - \text{DOX unentrapped (wt)}}{\text{Total DOX added (wt)}} \times 100 \quad (2)$$

## Drug release investigation

To investigate the in vitro drug release, GO@PEG/Au/Apt (DOX) solution (1 wt.%) was transferred to 2.0-mL vials against phosphate buffer (pH 6.6, pH 7.4). At predefined intervals, the buffer solution at the vials was collected for UV–Vis analysis at 488 nm and replaced with fresh buffer solution. The percentage of drug release was calculated using Eq. (3):

$$\%\ \text{Drug release} = \frac{\text{Drug release concentration}}{\text{Drug loading concentration}} \times 100 \quad (3)$$

## Cell viability assay

Cell viability was measured by MTT assay. Briefly, MCF-7, HT-29, and Hep-G2 were cultured in DMEM media with 10% (*v*/*v*) FBS, 1% pen/strep, 1% L-glutamine, and 1% NEAA. The cells were incubated at 37 °C in a humidified incubator containing 4% $CO_2$ in 25 $cm^3$ tissue culture-treated flasks. MCF-7, HT-29, and Hep-G2 ($10^4$ cells/ well) were seeded in 96-well plates in full medium and were incubated overnight at 37 °C. Three cell lines were then treated with GO@PEG/Au/Apt and GO@PEG/Au/Apt (DOX) at different concentrations (5.0, 7.5, 10.0, 15.0, and 20.0 μg $mL^{-1}$) for 48 h. Free DOX (19.8 μg $mL^{-1}$) and untreated cells were considered as positive and negative controls, respectively. After 48 h, the supernatant was removed and cell pellet washed immediately with PBS. Then, an aliquot of 90 μL DMEM and 10 μL MTT stock solution were subsequently added to each well and incubated for 4 h at 37 °C. MTT solution was then removed and 100 μL of DMSO added to each well and incubated for 40 min at 37 °C. Finally, the absorbance was read at 490 nm with an ELISA reader (Bio-Rad USA), and each experiment was performed in triplicate.

## Hemolysis assay

Hemolysis assay was used to investigate the biocompatibility of the synthesized cancer nanotheranostics system. Briefly, blood sample (1.0 mL) was centrifuged at 1500 rpm for 5 min and washed three times with PBS separating the supernatant from pellets. Then 200 mL of washed blood was completely mixed with 4.0 mL of PBS. Diluted blood solutions (200 μL) were added to 800 μL of different concentrations of the sample (GO@PEG/Au/Apt (DOX)—5, 7.5, 10, 15, and 20 μg $mL^{-1}$) and vortexed slowly. Pure water and PBS were used as a positive and negative control, respectively. The vials were kept at room temperature for 2 h and then were centrifuged at 1600 rpm for 5 min. The absorption of supernatant fluid was then read at 541 nm by spectrophotometry (Jenway 7315, UK) to determine the hemolysis. The percentage of hemolysis was calculated using Eq. (4):

$$\%\text{Percent hemolysis} = \frac{\text{Sample absorbance–Negative control absorbance}}{\text{Positive control absorbance–Negative control absorbance}} \quad (4)$$

## Cell imaging

MCF-7, HT-29, and Hep-G2 cells were cultured in DMEM media with 10% (*v*/*v*) FBS, 1% pen/strep, 1% L-glutamine, and 1% NEAA and were allowed to adhere to the glass cover slip in a 12-well plate for 24 h ($10^5$ cells/well). The cells were then exposed to 5 μg $mL^{-1}$ of GO@PEG/Au/Apt (DOX) for 2 h at 37 °C. The culture medium was then aspirated and cells were washed three times with PBS removing the excess nanosystem. The obtained samples were finally fixed with 4 wt.% paraformaldehyde in PBS for 15 min. The experiment was performed in triplicate for statistical analysis.

## ICP-OES analysis

Intracellular uptake behavior of the targeted (GO@PEG/Au/Apt) and non-targeted (GO@PEG/Au) nanosystem was investigated using an ICP-OES, in which the known number of cells from each sample was analyzed regarding their gold content. Three cell lines were cultured in 24-well plates at the concentration of $5 \times 10^4$ cells/well for 24 h. Cells were then exposed to 5 and 20 μg $mL^{-1}$ of GO@PEG/Au and GO@PEG/Au/Apt for 24 h. Then, cells were washed with PBS and digested with Trypsin enzyme followed by centrifugation at 1500 rpm for 5 min. After removing the supernatant, cells were dispersed in PBS and the same concentrations ($75 \times 10^3$ cells) of each cell lines were mixed with 2 μL hydrochloric acid (HCl). The samples were then incubated at 37 °C for 1 h and were stored at 24 °C for 24 h. Finally, samples were analyzed with ICP-OES to quantify the gold content (ppb). The experiments were performed in triplicate.

## Flow cytometry analysis

In order to assess the internalization of DOX, flow cytometry analysis was performed. MCF-7, HT-29, and HepG2 cells were cultured in 24-well plates for 24 h ($5 \times 10^4$ cells/well). The cells were then exposed to 5.0 μg $mL^{-1}$ of DOX (positive control), GO@PEG/Au/Apt (negative control), and GO@PEG/Au/Apt (DOX) (containing 4.95 μg $mL^{-1}$ of DOX) for 24 h at 37 °C. After that, cells were washed with PBS and were digested with enzyme followed by centrifugation at 1500 rpm for 5 min. After removing the supernatant, the cells were dispersed in PBS. The fluorescence of DOX in the red region was used to detect the localization of DOX in the cells. The experiment was performed in triplicate.

# Results and discussion

Scheme 1 demonstrates a schematic of overall procedures in the synthesis of the presented cancer nanotheranostics system. Accordingly, in the present study, the GO was used as a nanocarrier and autofluorescence agent due to its high mechanical strength, photo-stability, easy surface modification, and excitation-wavelength-dependent photoluminescence (PL) with the widespread fluorescence from visible to NIR range that make it appropriate for drug delivery and bioimaging purposes. The major concern limiting the use of GO in biomedical applications is its unpredictable toxicity. Nevertheless, certain modifications are essential to improve the biocompatibility of GO inside the living organisms. Herein, we modified GO with PEG to increase the hydrophilicity of the GO, reducing the steric hindrance between the targeting ligand and biomarker, and reducing the overall systemic toxicity. Since AuNPs are potentially applicable as a direct fluorescence imaging system and had a large absorption cross-section bond overlapping with GO spectrum, where the emission peaks shifted from UV to NIR region, it can improve the detected GO fluorescence behavior [50, 51]. Therefore, using AuNPs in this system can assist the high-sensitivity recognition of biomarkers. Besides, the presence of targeted aptamer (MUC-1) in this system allows ultra-sensitive detection of biomarkers and increase therapeutic efficiency. Eventually, to achieve the therapeutic target, DOX was loaded onto the final nanosystem.

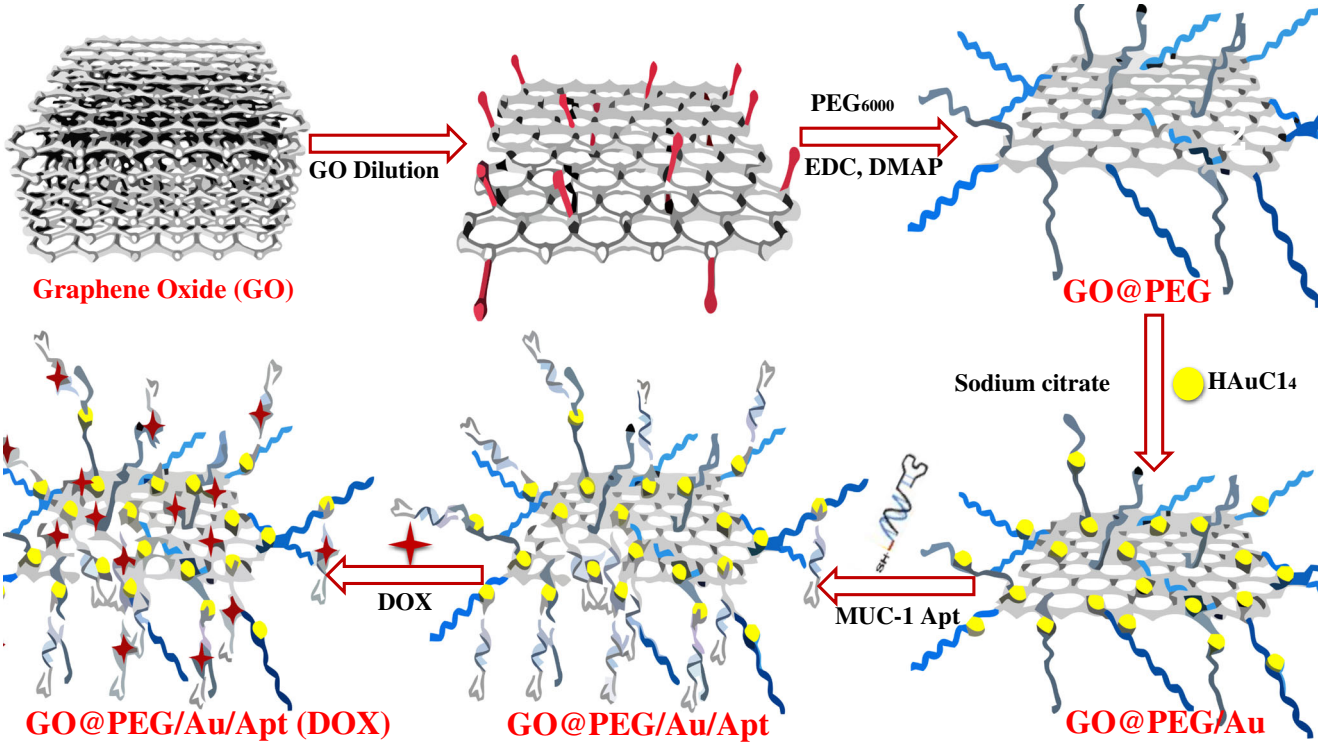


**Scheme 1** The schematic of nanosystem synthesis

## Characterization

### *PEGylated graphene oxide (GO@PEG)*

The chemical composition and interfacial interaction of the GO@PEG nano-conjugate were investigated utilizing FTIR. Figure 1a shows the FT-IR spectra of GO, PEG, and GO@PEG. According to the FT-IR spectrum of GO, the broad band at 3424 $cm^{-1}$ is attributed to the stretching vibrations of the O–H groups [52], while the peak at 1737 $cm^{-1}$ corresponds to the stretching vibrations of C=O of the carbonyl and carboxyl groups [53]. The spectrum of pure PEG is characterized by the stretching vibration of the C–H at 2847 $cm^{-1}$, the C–O bending vibration at 1104 $cm^{-1}$, the deformation vibration of the C–H bonds at 1468 and 1342 $cm^{-1}$, the bending vibration of the O–H at 1280 and 1242 $cm^{-1}$, and the C–O stretching vibration at 1149 $cm^{-1}$ [54]. The main absorption peaks of PEG and GO are preserved in GO@PEG with a slight shift in peak positions and changes relative in intensity. In addition, since there are C=O and O–H groups in GO and PEG, respectively, FTIR shows the ester bonding between carboxyl groups of GO and hydroxyl group of PEG after GO surface acylation using EDC and DMAP reducers.

The crystalline phase of GO, PEG, and GO@PEG were investigated using an X-ray diffractometer and the obtained results displayed in Fig. 1b. The XRD pattern of the pure GO was recognized based on a sharp diffraction peak at $2\theta =$ 10.4°, corresponding to the (001) crystalline plane diffraction peak of GO [55]. The XRD diffraction pattern of PEG was confirmed by the characteristic diffraction peaks at 19.2°, 23.3°, and 26.4° [54], whereas the XRD diffraction pattern of GO@PEG was broad at $2\theta = 15°$ and 29°, indicating that the obtained nano-conjugate has become more amorphous [55]. It is shown that the GO has a significant influence on the arrangement of the PEG molecular chain in the polymer crystal lattice, destroying its crystalline order and crystallinity confirms an effective conjugation of PEG to GO nanosheets through ester bonding.

To measure the thermal stabilities of pure GO and GO@PEG, TGA was applied by heating the samples under a nitrogen atmosphere to 800 °C. The TGA curve of GO shown in Fig. 1c exhibited the first weight-loss stage below 100 °C due to the removal of physically adsorbed water. The second stage occurring around 180–220 °C attributed to pyrolysis of the oxygen-containing groups on GO sheets [56], when overall GO lost almost 40% of its total weight. In contrast, the TGA curves of GO@PEG demonstrated the main weight loss around a temperature range from 320 to 420 °C, attributed to the thermal degradation of the PEG chains and pyrolysis of the carbon skeleton in GO [56]. In addition, the weight loss around 180–220 °C is associated with the degradation of more stable oxygen functionalities in the GO [57]. Based on these results, the content of grafted polymer was estimated about 55 wt.%, making the nano-conjugate more water soluble, stable, and biocompatible, promoting the synthesized modified GO as a platform for cancer simultaneous imaging and therapy.

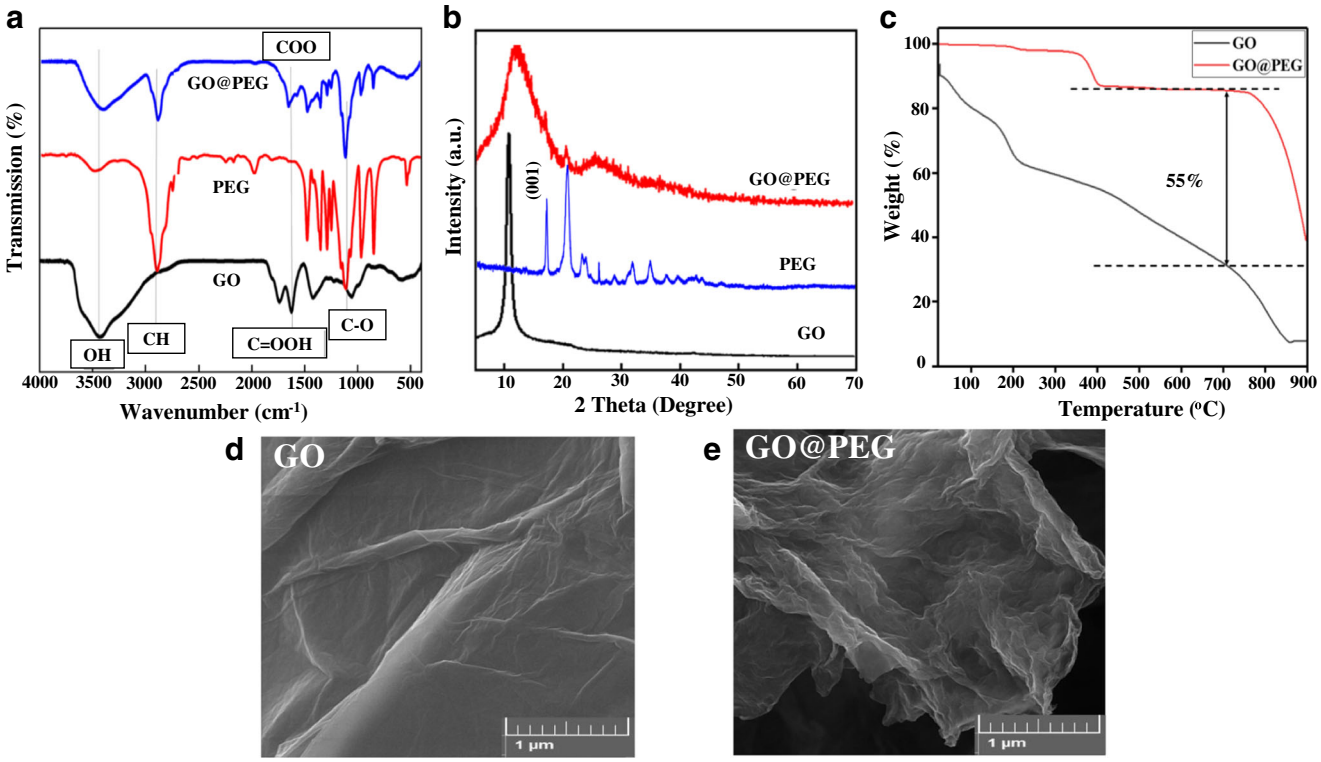


**Fig. 1** **a** FT-IR spectra of GO, PEG, and GO@PEG; **b** XRD patterns of GO, PEG, and GO@PEG; **c** TGA data recorded for GO and GO@PEG nano-conjugate; **d** FE-SEM images of GO and **e** GO@PEG

The morphology of the GO and GO@PEG was studied using FE-SEM showing that the GO has a layered distribution, stacking together in a flocculent manner (Fig. 1d). The surface is relatively flat and the edges are more obvious. As the FE-SEM image of GO@PEG (Fig. 1e) shows, the edges are curled into an irregular shape due to the intermolecular ester bonding.

### GO@PEG/Au

The crystallographic structure of the prepared GO@PEG/Au was studied using XRD (Fig. 2a). The distinguished peaks at 38.2°, 44.59°, and 64.7° correspond to the (220), (200), and (111) planes, respectively, confirming the formation of Au nanoparticles (AuNPs) on the nano-conjugate [58]. Considerably, the connection between some AuNPs and GO sheets or PEG chains results in the weak peaks of Au at the obtained graphs.

Figure 2b shows the FE-SEM micrographs of GO@PEG/Au. The selected area has indicated the uniform dispersion of AuNPs at the entire surface of GO@PEG with an average size of ~ 15–20 nm. To characterize the chemical composition of GO@PEG/Au, EDX analysis was utilized. A meaningful picture of element distribution on the surface verified the presence of carbon, oxygen, and gold elements throughout the surface of GO@PEG/Au (Fig. 2c). EDX spectra represented in Fig. 2d further showed the related peaks of carbon (C), oxygen (O), and gold (Au) at the final conjugate.

### GO@PEG/Au/Apt (DOX)

The designed MUC-1 aptamer (Apt) is composed of one (Apt-L1) or three (Apt-L3) loop sequences with three important parts that were described in our previous study [49]: (1) a thiol linking the aptamers to the AuNPs by formation of thiol–Au bonds; (2) molecular docking and the binding sites of the drug interacting with Apt-L1 and Apt-L3, respectively; (3) an aptamer loop segment to specifically bind target tumor cells. The designed aptamer was conjugated to the surface of GO@PEG/Au to selectively target the MUC-1 biomarker on the particular tumor cells.

According to the FT-IR spectrum of GO@PEG/Au/Apt, the broad band at 621 $cm^{-1}$, attributed to the heterocyclic groups of the aptamers, confirms the successful conjugation of Apt to the surface of GO@PEG/Au (Fig. 3a). Moreover, the decreased intensity of the CC–H band at 955 $cm^{-1}$ indicated the effective graft of Apt on the obtained nano-conjugate [59, 60]. The appearance of GO@PEG/Au/Apt has been changed compared with GO@PEG/Au, considering the FE-SEM results (Fig. 3b). EDX analysis also provided a meaningful picture of element distribution on the surface of nano-conjugate, verifying the presence of sulfur element which linked at the end of Apt (Fig. 3c). EDX spectra illustrated

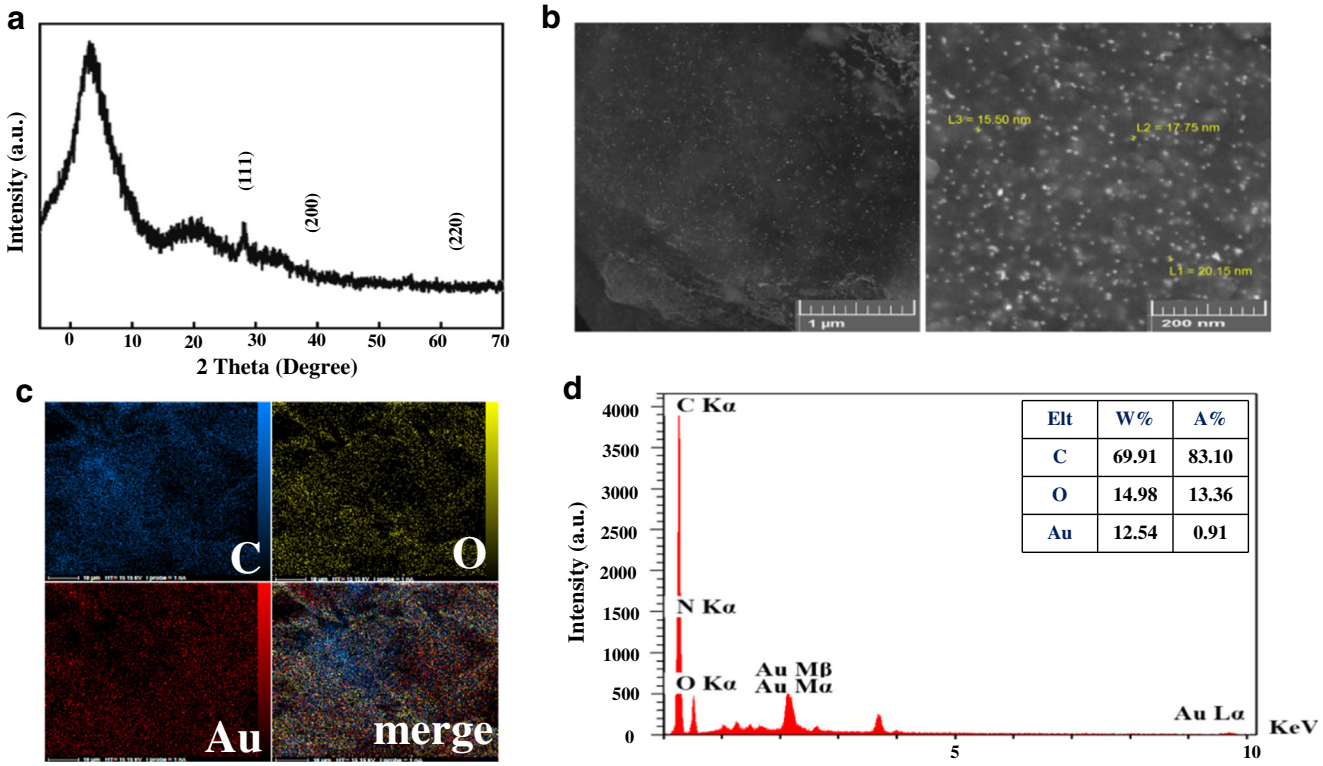


**Fig. 2** **a** XRD patterns of GO@PEG/Au nano-conjugate; **b** FE-SEM images of GO@PEG/Au nano-conjugate showing AuNP distribution and their average sizes on the surface of GO@PEG; **c** EDX mapping and **d** EDS analysis indicating the element distribution on the surface of GO@PEG/Au

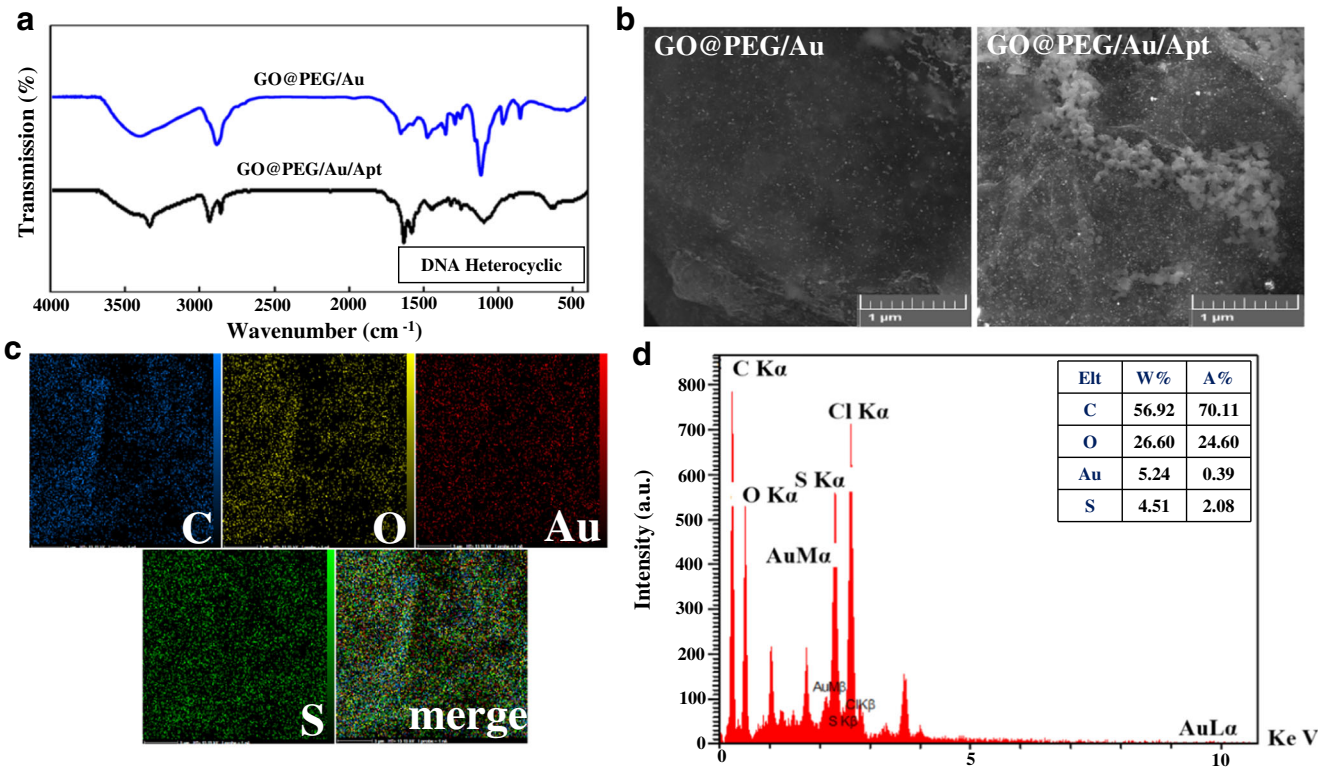


**Fig. 3** **a** FT-IR analysis of GO@PEG/Au/Apt nano-conjugate; **b** FE-SEM images of GO@PEG/Au and GO@PEG/Au/Apt nano-conjugates; **c** EDX mapping and **d** EDS analysis illustrating the element distribution on the surface of GO@PEG/Au/Apt

the related peaks of C, O, Au, and sulfur (S) on the conjugate (Fig. 3d).

Loading DOX, an effective anticancer drug, into nano-conjugate was done as the last step of the synthesis. DOX either intercalates into the double-stranded regions of the aptamers through non-covalent intercalation or is adsorbed on the GO surface via π-π stacking and hydrophobic interactions [61, 62]. The DOX-loading capacity and the entrapment efficiency were calculated based on adsorption of free DOX after loading measured based on the standard curve of DOX/phosphate buffer (Fig. S1), in which the amount of entrapped and loaded DOX was about 99.96%.

Besides, the zeta-potential analysis was utilized as the last characterization analysis to assay the nano-conjugate surface charge in each synthesis step (Fig. S2). The zeta potential of GO@PEG at − 12.3 mV indicates the negative charge of the conjugate. The obtained GO@PEG/Au after modification with Au NPs makes zeta potential more negative to − 13.2 mV due to the presence of sodium citrate carboxyl groups. The connection between aptamers and Au NPs increased zeta potential negatively to −20.9 mV due to the negative charge of DNA. The conjugate of DOX altered the zeta potential to − 4.49 mV, simply due to its positive charge. These results confirmed the effective loading of DOX onto the GO@PEG/Au/Apt nano-conjugate.

## In vitro bioactivity study

### DOX release

The pH-responsive release of DOX was studied at two different pH (7.4 and 6.6), considering the normal and tumor physiological conditions (Fig. 4a). The release pattern is separated into three parts: (1) burst release of DOX at first 3 h, the physically associated DOX at the nano-conjugate surface; (2) first sustained release, attributed to the drugs presented on the GO surface and PEG chains; (3) second sustained release, related to the drug molecules located between the two strands of aptamer. The total drug release of 47 and 62% at pH values of 7.4 and 6.6 were measured during 10 days, respectively. The accelerated release at acidic conditions might be attributed to the protonation of the existed $–NH_2$ groups on DOX molecule. Therefore, the hydrophobicity and solubility of DOX increase as well as reducing the hydrophobic interaction between DOX and nano-conjugate. In addition, comparing the mean percentage release in the above three stages confirmed that more than 50% of release occurred specifically in the last stage. To reduce the nonspecific release of nano-conjugates, it was used after washing three times with PBS.

### Sensitivity and selectivity study

MTT analysis was performed to evaluate the specific cell toxicity and targeted therapy of the cancer nano-theranostic system. For this purpose, GO@PEG/Au/Apt, GO@PEG/Au/Apt (DOX), and free DOX were used to treat the three different cell lines. Considering Fig. 4b, all the treated cell lines show no appreciable viability loss after treatment with a variety of GO@PEG/Au/Apt concentrations. These results demonstrate the excellent biocompatibility of the synthesized nano-conjugate. The cytotoxicity of the parent DOX and GO@PEG/Au/Apt (DOX) was then investigated. According to the MTT results shown in Fig. 4c, non-selective cytotoxicity of parent DOX (20 μg $mL^{-1}$) on the three cell lines indicates its adverse side effects on normal tissues. While the toxicity of the GO@PEG/Au/Apt (DOX) at all concentrations in MCF-7 and HT-29 cells (as overexpression MUC-1 receptor cell line) are significantly higher than Hep-G2 (as negative control cell line). These results show the efficiency of the proposed system for transporting the chemotherapeutic drugs into the desired tumor cells as a cancer nanotheranostic carrier. Besides, based on results, 5.0 μg $mL^{-1}$ concentration of the nano-conjugate showed a significant difference in toxicity in both positive and negative tumor cells. Therefore, this concentration of nano-conjugate (5.0 μg $mL^{-1}$) was introduced as an optimum concentration to be used for further studies.

Furthermore, the effect of MUC-1 aptamer on the cellular uptake of nano-system was investigated based on Au element uptake in the MUC-1-positive cells (MCF-7 and HT-29) and MUC-1-negative cells (Hep-G2), using ICP-OES analysis. To this end, the uptake efficiency of GO@PEG/Au and GO@PEG/Au/Apt (with two concentrations—5, 20 μg $mL^{-1}$) were evaluated. Considering Fig. 4d, the uptake of the GO@PEG/Au/Apt conjugate by MCF-7 and HT-29 cells is significantly higher than Hep-G2. Likewise, the uptake of the GO@PEG/Au/Apt conjugate by positive cells has significantly increased compared with GO@PEG/Au conjugate. These results confirm that this nano-conjugate can be selectively taken up by the MUC-1 biomarker with high affinity and ensure of its selectivity for delivery of toxic cargo such as DOX.

### Hemolysis assay

As an intravenous injectable drug carrier, the effect of GO@PEG/Au/Apt (DOX) on RBC was further evaluated, using hemolytic assay. The results represented in Fig. 4e showed only less than 1% hemolysis of RBC when introduced to the various concentrations of GO@PEG/Au/Apt (DOX). So, according to the American Society for Testing and Materials (ASTM F 756-00, 2000), GO@PEG/Au/Apt (DOX) is considered as a hemo-compatible conjugate, even in the presence of drug molecules.

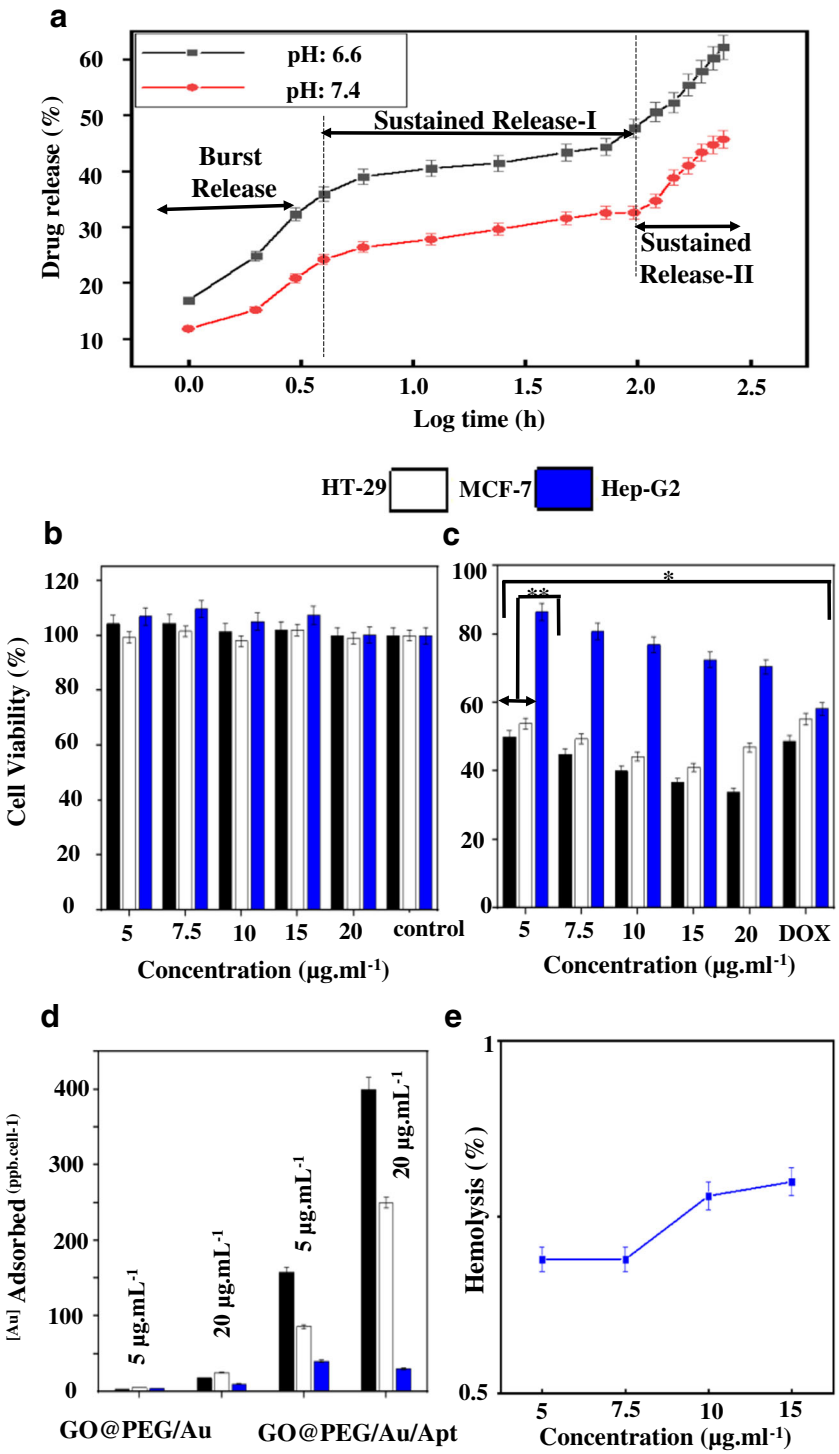


**Fig. 4** **a** Nano-conjugate drug release at two different pH values. Viability assay of HT-29, MCF-7 (target cells), and Hep-G2 (control cells) treated with different concentration of **b** GO@PEG/Au/Apt and **c** GO@PEG/Au/Apt (DOX) and free DOX with 19.8 μg $mL^{-1}$ concentration. Each test was repeated three times and the significant samples are determined by "*" and the concentration with significant toxicity in positive and negative cell lines is determined by "**"; **d** cellular uptake of GO@PEG/Au and GO@PEG/Au/Apt (5 and 20 μg $mL^{-1}$) in MCF-7, HT-29, and Hep-G2 cell lines; **e** hemolysis experiment shows the hemo-compatibility of nano-conjugate

## Fluorescence study

The fluorescence behavior of each component present in the synthesized nano-conjugate was evaluated through the fluorescence spectroscopy, and the details are explained in the supplementary information. Briefly, the results indicated that GO has the broad emission spectrum from 200 to 800 nm, in which the maximum intensity of the emitted fluorescence detected at excitation wavelength of λex: 300 nm, with emissions peaked at λem: 595 nm (Fig. S3A). On the other hand, we demonstrated a continuous emission spectrum of PEG6000 with good intensity at the range of 200–500 nm for the first time (Fig. S3B). Likewise, the maximum intensity of the emitted fluorescence occurs at the excitation wavelength of λex: 300 nm, with emissions peaked at λem: 582, 590, and 605 nm. The synthesized AuNPs with the sizes ranges from 10 to 15 nm have a

high fluorescence intensity with sharp emission peak, which makes them proper as the sensing signal (fluorescent biosensors). Besides, AuNPs exhibited an emission spectrum in the range of 200–600 nm, in which the maximum intensity detected at excitation wavelength was 300 nm (λex = 300 nm, λem = 585 nm), as shown in Fig. S3C**.** Fluorescence property of the modified GO with PEG molecule (GO@PEG) and AuNPs (GO@PEG/Au) were further investigated. Considering Fig. S3D and E, both conjugates show high fluorescence intensity, in which the maximum intensity occurs at an excitation wavelength of 300 nm, with emission peaks at λem: 370, 597 nm.

Furthermore, the fluorescence intensity investigations of nano-conjugate by fluorescence microscopy shown in Fig. 5a confirmed the obtained results from the fluorescence spectroscopy; the fluorescence of GO was decreased in GO-PEG, while the AuNPs conjugation increased the GO fluorescence. Several studies have shown that GO or AuNP can quench the emitted fluorescence. As an energy donor in FRET, GO is quenched by AuNPs. It requires the donor's emission energy overlap the acceptor's absorption spectrum. For this purpose, the donor and the acceptor need to be so closed to each other (Förster radius = 6 nm). On the other hand, if GO acts as an energy acceptor, it quenches the fluorescence of AuNPs, while the effective quenching distance (Förster radius) extends to around 30 nm. In the present study, the fluorescence properties of both components (GO and AuNPs) in the final conjugate have been preserved with good intensity. This could be due to the presence of PEG chains, which extends the distance between the two fluorophores.

Moreover, the present study represented the capability of GO, GO@PEG, and GO@PEG/Au to emit in three fluorescence regions (blue, green, and red). Since all structural components of this conjugate are highly fluorescing at excitation wavelength of 300 nm (Fig. 5b), the fluorescence behavior of nano-conjugate at the same wavelength was further evaluated.

From Fig. 6a, GO acts as an energy acceptor in GO@PEG, quenching the fluorescence of PEG as an energy donor at λem: 588 and 605 nm emission wavelengths. On the other hand, the fluorescence of GO was also quenched at the range of λem: 450–550 nm and λem: 650–750 nm as GO acts as a charge donor. Based on these results, GO can act as an energy acceptor and charge donor simultaneously. In other words, this shows the potential of GO not only as a fluorophore but also as a quencher at the same system. This provides new opportunities for the development of innovative fluorescence biosensors and bio-imaging systems detecting multiple biomarkers on a single biosensor. On the other hand, conjugation of AuNPs to GO@PEG is represented in Fig. 6b, increasing the fluorescence intensity as well as emerging two new emission peaks at 390 (blueshift) and 742 nm (redshift). Since the performance of detecting imaging signals is limited by the broad fluorescence of GO, the narrow fluorescence of GO@PEG/Au in three fluorescence regions (blue, green, and red) makes this system ideal for bio-imaging applications. In fact, AuNPs cause plasmon-enhanced fluorescence once conjugated to a fluorophore within an optimal separation distance (5 nm). Due to the charge transfer from nano-conjugate to Apt, a two-stranded aptamer quenches the GO@PEG/Au fluorescence, creating an "on/off" fluorescence biosensor (Fig. 6c). In other words, the energy transfer occurred between the base pairs in the hairpin of dsDNA aptamer and GO results in a lower fluorescence intensity. The specific binding of

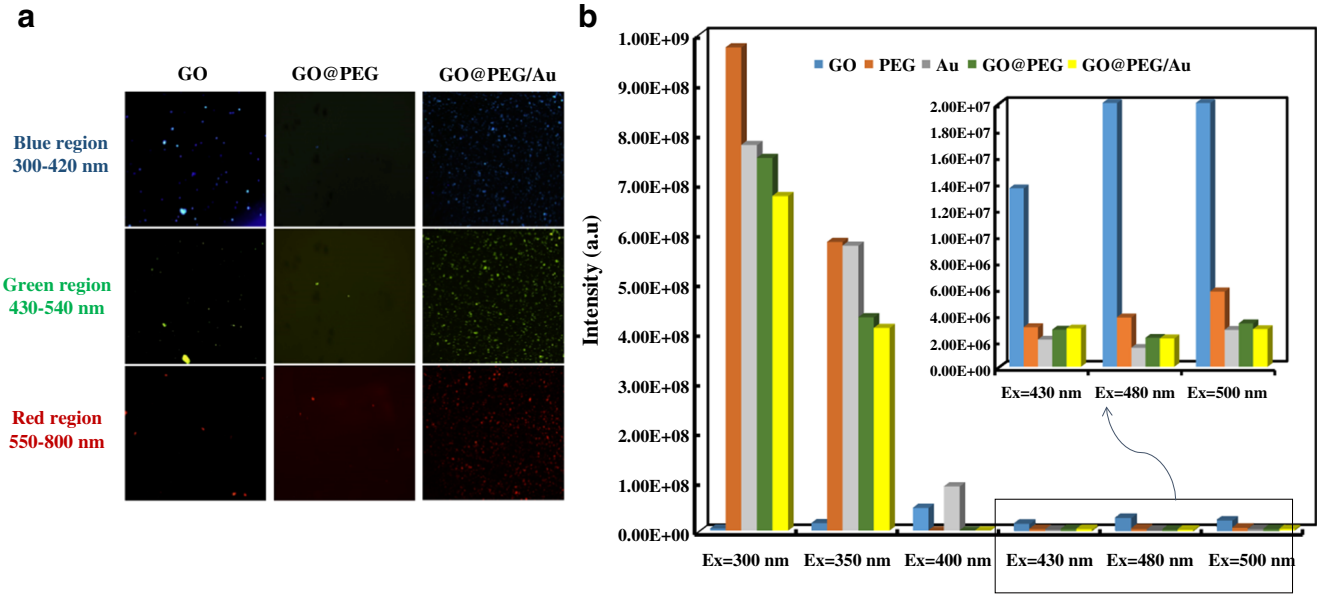


**Fig. 5** **a** Fluorescence properties of GO, GO@PEG, and GO@PEG/Au, observed by fluorescence microscopy; **b** fluorescence intensity of the components at GO@PEG/Au/Apt in different excitation range

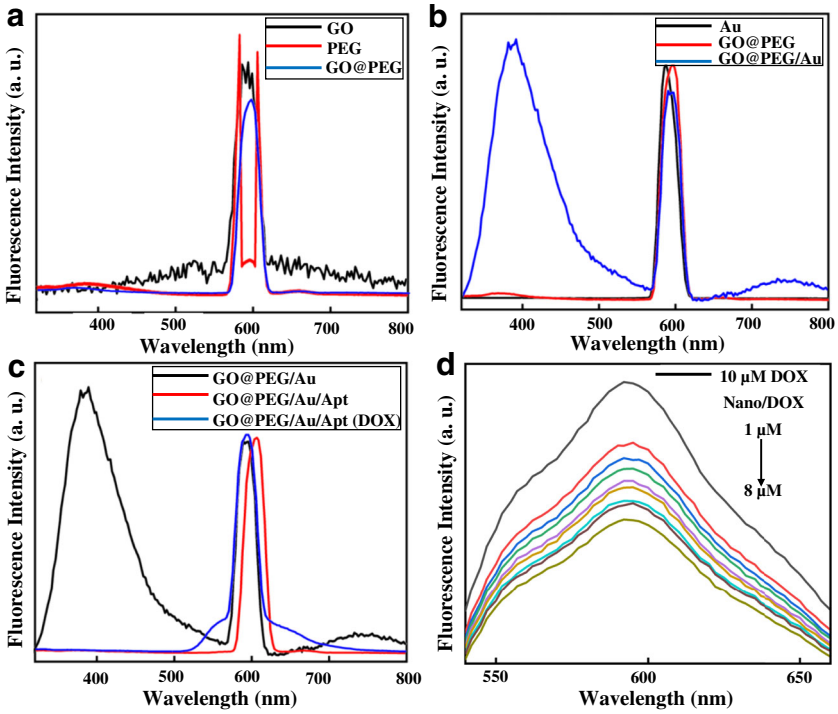


**Fig. 6** **a**–**c** Fluorescence behavior of nano-conjugate in the each synthesized step; **d** the interaction of DOX and different concentrations of nano-conjugate (1–8 μg $mL^{-1}$).

aptamer to the MUC-1 receptor leads to the separation of the two strands, recovering the fluorescence signal to produce an "On" state. Therefore, the synthesized GO@PEG/Au could be applicable for fluorescence imaging study and plays a key role in targeted delivery and definite therapy.

The interaction of DOX with different concentrations of nano-conjugate (1–8 μg $mL^{-1}$) was also monitored using fluorescence spectroscopy with excitation wavelength of 488 nm. The results in Fig. 6d revealed that the emission of DOX is gradually quenched by increasing the concentration of GO@PEG/Au/Apt, representing Apt as a quencher.

## Targeted imaging study

The ability of the GO@PEG/Au/Apt(DOX) nano-conjugate as the labeling agent was evaluated using fluorescent microscopy utilizing the inherent fluorescence properties of the GO@PEG/Au. It is assumed when the aptamer specifically binds to the MUC-1 receptor, the double strands of aptamer separates resulting in drug release and reversing the fluorescence properties of the GO@PEG/Au. From the fluorescent images of the tumor cells (Fig. 7a), the fluorescence intensity of the nano-conjugate in the desired cells (MCF-7 and HT-29) is significantly higher than the control cells (Hep-G2). In addition, it is evident that the nano-conjugate shows fluorescence emission in three regions (blue, green, and red) in in vitro conditions. Based on these results, the synthesized GO@PEG/Au/Apt (DOX) exhibits cell specificity which selectively taken up by the MUC-1-positive cells.

## Targeted drug delivery study

To determine the targeting properties of GO@PEG/Au/Apt (DOX) and drug delivery efficiency, the three cell lines have been treated with both free DOX and drug-loaded carrier (GO@PEG/Au/Apt (DOX)). Flow cytometry analysis was applied to evaluate the nano-conjugate uptake by the MUC-1-positive and MUC-1-negative cells. As shown in Fig. 7b, 98% of free drug was uptaken by all three cell lines (MCF-7, HT-29, Hep-G2) based on the fluorescent signals generated by free DOX, whereas the drug uptake of GO@PEG/Au/Apt (DOX) for MUC-1-positive HT-29 and MCF-7 cells is about 68.24 and 54.10%, respectively. For MUC-1-negative HepG2 cells, however, the fluorescent signal generated by GO@PEG/Au/Apt (DOX) is remarkably lower to about 11%. Thus, these results confirm that GO@PEG/Au/Apt (DOX) is selectively taken up by the MUC-1-positive tumor cells, and the intercalation of DOX within the MUC-1 aptamer does not affect its binding properties. Likewise, the comparison between free DOX and GO@PEG/Au/Apt (DOX) uptake demonstrated the targeted and controlled drug delivery.

Considering all the obtained results, GO@PEG/Au/Apt (DOX) deserves to be introduced as a cancer nanotheranostics system for simultaneous non-invasive fluorescence imaging and targeted therapy. We have also compared our platform in the present study with recent best studies in this field and evaluated the advantages and disadvantages of our nano-system. The results are described in Table 1.

With reference to the aforementioned merits demonstrated in Table 1, our nanotheranostic platform has some advantages that

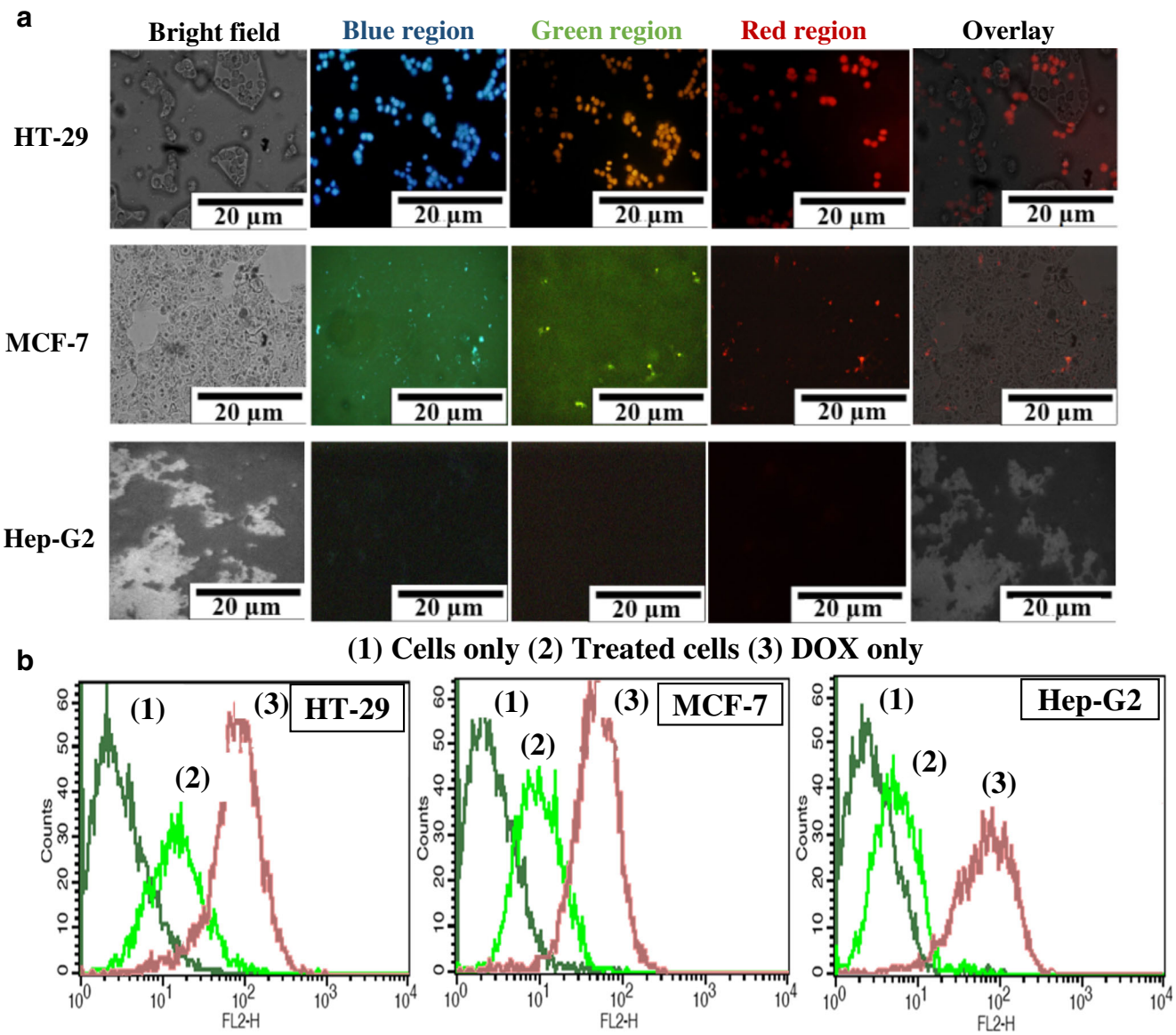


**Fig. 7** **a** Bright-field, fluorescent (blue, green, and red regions), and overlay microscopic images of HT-29, MCF-7, and Hep-G2 after incubation with GO@PEG/Au/Apt (DOX). **b** Flow cytometry histograms of the three mentioned cell lines after incubation with 20 μg $mL^{-1}$ of free DOX and 5 μg $mL^{-1}$ GO@PEG/Au/Apt (DOX)

make it noticeable, including (1) simultaneous presence of three fluorophore components (GO, PEG, and AuNPs), which preserve their fluorescence property with high intensity in the final detectable system (GO@PEG/Au), creating a switchable "on/off" biosensor; (2) non-invasive and low-cost detection technique with good efficiency in comparison with other optical detection; (3) the tunable fluorescence of the GO@PEG/Au conjugate between ultraviolet, visible, and NIR with a robust intensity, making it applicable in in vivo biomedical studies; and (4) the drug loading and release behavior of our platform compared with other similar studies showing much higher loading efficiency and better performance in response to the acidic environment of tumor tissue, which could be attributed to the three loading sites in the nanosystem.

It is noteworthy that our proposed nano-theranostic platform may also show some drawbacks. Two major limitations are as follows: (1) Due to the multi-layer structure of the nanosystem, the drug releasing in long term may be limited. (2) Due to the short lifespan of aptamer in the environment, the stability and maintenance of the nanosystem for long time is difficult.

## Conclusions

In summary, we developed a cancer nanotheranostic system GO@PEG/Au/Apt (DOX) that could selectively attach to the MUC1-positive breast and colon tumor cells in order to trace, image, and target the chemotherapy agents to the desired sites.

**Table 1** An overview on recently reported nanotheranostic platforms based on optical detection

| Nanotheranostic platform | Optical detection | Targeted agent | Advantages | Disadvantages | Reference |
|---|---|---|---|---|---|
| Au-rGO-CS-PpIX-FA | SERS | FA | – Strong light imaging<br>– Dual targeted therapy | – Relatively low drug loading capacity (60%)<br>– Expensive equipment for detection<br>– Multi-layer structure and limited drug release in long time | [63] |
| HG-GNCs/GO-5FU | Fluorescence | HA | – Tri-therapies | – Low drug loading efficiency (25.3%) | [64] |
| GO-Apt | Fluorescence | Apt | – High targeted detection<br>– High targeted apoptosis | – Using fluorescent label probe<br>– Short lifespan of aptamer | [65] |
| GO-CA-GD-Au | CT | – | – Dual imaging | – Non-targeted therapy and imaging<br>– Non-sustained drug release<br>– Multi-layer structure and limited drug release in long time | [66] |
| SiPc-GO | Fluorescence | – | – Dual efficient therapy | – Non-targeted therapy and imaging | [67] |
| Aptamer-Au@SPIONs | Fluorescence | Apt | – Targeted imaging and therapy | – Using fluorescent label probe<br>– Short lifespan of aptamer | [68] |
| GO@PEG/Au/Apt | Fluorescence | Apt | – Autofluorescence platform<br>– Targeted imaging and therapy | – Multi-layer structure and limited drug release in long time<br>– Short lifespan of aptamer | This study |

Photosensitizer: PpIX, reduced graphene oxide: rGO, chitosan: CS, folic acid: FA, surface-enhanced Raman scattering: SERS, hyaluronic acid: HA, gold nanoparticles: GNCs, (HA)-glutathione (GSH): HG, chlorogenic acid: CA, gadolinium: Gd, silicon phthalocyanine: SiPc, superparamagnetic iron oxide nanoparticles: SPIONs

Interestingly, when the MUC-1 target on the specific cells (MCF-7 and HT-29) is introduced, due to the stronger binding affinity of the aptamer to its target, the aptamer prefers to form an aptamer–target complex rather than the dsDNA. Hence, the two strands of aptamer are separated, and slight fluorescence is obtained after the introduction of GO@PEG/Au due to the weak affinity of the generated mononucleotides to GO. Therefore, by monitoring the change of fluorescence signal, the target could be detected. The results of in vitro imaging study indicated a good fluorescence intensity of the platform in three fluorescence regions (blue, green, and red), introducing that as an "on/off" biosensor. Besides the biocompatibility of the GO@PEG/Au/Apt as a nanocarrier, the GO@PEG/Au/Apt (DOX) represented more cytotoxicity toward the targeted tumor cells in comparison with the non-targeted cells. The proposed platform is therefore applicable as a therapeutic agent reducing the dosage of drug, preventing drug resistance of tumor cells.

Considering the absorbance of GO and AuNPs at near-infrared region, further investigation is required to study the great potential of this platform in hyperthermia of the targeted tumor cells. Besides, due to the application of AuNPs in various imaging techniques (photoacoustic, CT, SERS), this platform is ideal for multimodal imaging, in which fluorescence imaging combines with other imaging modalities, such as CT. This strategy would be assessed in future work, as a powerful tool to improve the sensitivity and accuracy, which are critical in improved cancer diagnosis and treatment. Moreover, based on the type of aptamer and chemotherapeutic agent, this nanotheranostic platform has the potential to be used for the detection and treatment of various tumors. Overall, it is suggested that GO@PEG/Au/Apt (DOX) may have great latent potentials in biomedical applications achieving the precision medicine goals.

## Compliance with ethical standards

**Conflict of interest** The authors declare that they have no conflict of interest.

## References

1. Mendes LP, Lima EM, Torchilin VP (2018) Targeted nanotheranostics for selective drug delivery in cancer. In: Handbook of nanomaterials for cancer theranostics. Elsevier. p. 245–277
2. Khorrami S, Zarrabi A, Khaleghi M, Danaei M, Mozafari MR (2018) Selective cytotoxicity of green synthesized silver nanoparticles against the MCF-7 tumor cell line and their enhanced antioxidant and antimicrobial properties. Int J Nanomedicine 13:8013–8024
3. Zarepour A, Zarrabi A, Larsen KL (2019) Fabricating B-cyclodextrin based pH-responsive nanotheranostics as a programmable polymeric nanocapsule for simultaneous diagnosis and therapy. Int J Nanomedicine 14:7017–7038
4. Miyake M, Sugano K, Sugino H, Imai K, Matsumoto E, Maeda K, Fukuzono S, Ichikawa H, Kawashima K, Hirabayashi K, Kodama T, Fujimoto H, Kakizoe T, Kanai Y, Fujimoto K, Hirao Y (2010) Fibroblast growth factor receptor 3 mutation in voided urine is a useful diagnostic marker and significant indicator of tumor

recurrence in non-muscle invasive bladder cancer. Cancer Sci 101(1):250–258
5. Miao T et al (2019) Nanotheranostics-based imaging for cancer treatment monitoring, in nanotheranostics for cancer applications. Springer, pp 395–428
6. Bidram E, Esmaeili Y, Ranji-Burachaloo H, al-Zaubai N, Zarrabi A, Stewart A, Dunstan DE (2019) A concise review on cancer treatment methods and delivery systems. Journal of Drug Delivery Science and Technology 54:101350
7. Wang Y, Wang S, Lu C, Yang X (2018) Three kinds of DNA-directed nanoclusters cooperating with graphene oxide for assaying mucin 1, carcinoembryonic antigen and cancer antigen 125. Sensors Actuators B Chem 262:9–16
8. Nielsen LJ, Olsen LF, Ozalp VC (2010) Aptamers embedded in polyacrylamide nanoparticles: a tool for in vivo metabolite sensing. ACS Nano 4(8):4361–4370
9. Shoghi E, Mirahmadi-Zare SZ, Ghasemi R, Asghari M, Poorebrahim M, Nasr-Esfahani MH (2018) Nanosized aptameric cavities imprinted on the surface of magnetic nanoparticles for high-throughput protein recognition. Microchim Acta 185(4):241
10. Zhou J, Rossi J (2017) Aptamers as targeted therapeutics: current potential and challenges. Nat Rev Drug Discov 16(3):181–202
11. Miao Q, Pu K (2018) Organic semiconducting agents for deep-tissue molecular imaging: second near-infrared fluorescence, self-luminescence, and photoacoustics. Adv Mater 30(49):1801778
12. Daniel A, Oron D, Silberberg Y (2019) Noninvasive linear fluorescence imaging through scattering media via wavefront shaping. arXiv preprint arXiv:1904.02509
13. Diao S, Blackburn JL, Hong G, Antaris AL, Chang J, Wu JZ, Zhang B, Cheng K, Kuo CJ, Dai H (2015) Fluorescence imaging in vivo at wavelengths beyond 1500 nm. Angew Chem Int Ed 54(49):14758–14762
14. Owens EA, Henary M, el Fakhri G, Choi HS (2016) Tissue-specific near-infrared fluorescence imaging. Acc Chem Res 49(9):1731–1740
15. Li C, Wang Q (2018) Challenges and opportunities for intravital near-infrared fluorescence imaging technology in the second transparency window. ACS Nano 12(10):9654–9659
16. Carr JA, Franke D, Caram JR, Perkinson CF, Saif M, Askoxylakis V, Datta M, Fukumura D, Jain RK, Bawendi MG, Bruns OT (2018) Shortwave infrared fluorescence imaging with the clinically approved near-infrared dye indocyanine green. Proc Natl Acad Sci 115(17):4465–4470
17. Li B, Lu L, Zhao M, Lei Z, Zhang F (2018) An efficient 1064 nm NIR-II excitation fluorescent molecular dye for deep-tissue high-resolution dynamic bioimaging. Angew Chem Int Ed 57(25):7483–7487
18. Shcherbakova DM, Stepanenko OV, Turoverov KK, Verkhusha VV (2018) Near-infrared fluorescent proteins: multiplexing and optogenetics across scales. Trends Biotechnol 36:1230–1243
19. Martinić I, Eliseeva SV, Petoud S (2017) Near-infrared emitting probes for biological imaging: organic fluorophores, quantum dots, fluorescent proteins, lanthanide (III) complexes and nanomaterials. J Lumin 189:19–43
20. Kim D, Kim J, Park YI, Lee N, Hyeon T (2018) Recent development of inorganic nanoparticles for biomedical imaging. ACS central science 4(3):324–336
21. Wegner KD, Hildebrandt N (2015) Quantum dots: bright and versatile in vitro and in vivo fluorescence imaging biosensors. Chem Soc Rev 44(14):4792–4834
22. Bruns OT, Bischof TS, Harris DK, Franke D, Shi Y, Riedemann L, Bartelt A, Jaworski FB, Carr JA, Rowlands CJ, Wilson MWB, Chen O, Wei H, Hwang GW, Montana DM, Coropceanu I, Achorn OB, Kloepper J, Heeren J, So PTC, Fukumura D, Jensen KF, Jain RK, Bawendi MG (2017) Next-generation in vivo optical imaging with short-wave infrared quantum dots. Nature biomedical engineering 1(4):0056
23. Du J et al (2019) Thiol-activated fluorescent probe for sensitive detection and imaging of proteins. Sensors Actuators B Chem 287:118–123
24. Qian X, Xu Z (2015) Fluorescence imaging of metal ions implicated in diseases. Chem Soc Rev 44(14):4487–4493
25. Dong J, Wang K, Sun L, Sun B, Yang M, Chen H, Wang Y, Sun J, Dong L (2018) Application of graphene quantum dots for simultaneous fluorescence imaging and tumor-targeted drug delivery. Sensors Actuators B Chem 256:616–623
26. de Lazaro I, et al (2018) Graphene oxide as 2D platform for complexation and intracellular delivery of siRNA. bioRxiv. 486522
27. Muñoz, R., et al., Graphene oxide for drug delivery and cancer therapy. In: Nanostructured polymer composites for biomedical applications. 2019, Elsevier. p. 447–488
28. Islami M, Zarrabi A, Tada S, Kawamoto M, Isoshima T, Ito Y (2018) Controlled quercetin release from high-capacity-loading hyperbranched polyglycerol-functionalized graphene oxide. Int J Nanomedicine 13:6059–6071
29. Li Y, Brennan JD, Liu M (2019) Reduced graphene oxide-based biosensors. Google Patents
30. Zeng L, et al (2018) Graphene oxide-based biosensors. In: Graphene oxide—applications and opportunities. IntechOpen
31. Yang J, Zhang Z, Yan G (2018) An aptamer-mediated CdSe/ZnS QDs@ graphene oxide composite fluorescent probe for specific detection of insulin. Sensors Actuators B Chem 255:2339–2346
32. Shareena TPD et al (2018) A review on graphene-based nanomaterials in biomedical applications and risks in environment and health. Nano-micro letters 10(3):53
33. Oh HJ et al (2018) Graphene-oxide quenching-based molecular beacon imaging for exosome-mediated transfer of neurogenic miRNA on microfluidic platform. Journal of Extracellular Vesicles 7:261–261
34. Srivastava S, Senguttuvan TD, Gupta BK (2018) Highly efficient fluorescence quenching with chemically exfoliated reduced graphene oxide. Journal of Vacuum Science & Technology B, Nanotechnology and Microelectronics: Materials, Processing, Measurement, and Phenomena **36**(4):04G104
35. Ye H, Lu Q, Duan N, Wang Z (2019) GO-amplified fluorescence polarization assay for high-sensitivity detection of aflatoxin B 1 with low dosage aptamer probe. Anal Bioanal Chem 411(5):1107–1115
36. Zheng P, Wu N (2017) Fluorescence and sensing applications of graphene oxide and graphene quantum dots: a review. Chemistry–An Asian Journal 12(18):2343–2353
37. He L, Li J, Xin JH (2015) A novel graphene oxide-based fluorescent nanosensor for selective detection of Fe3+ with a wide linear concentration and its application in logic gate. Biosens Bioelectron 70:69–73
38. Chien CT, Li SS, Lai WJ, Yeh YC, Chen HA, Chen IS, Chen LC, Chen KH, Nemoto T, Isoda S, Chen M, Fujita T, Eda G, Yamaguchi H, Chhowalla M, Chen CW (2012) Tunable photoluminescence from graphene oxide. Angew Chem Int Ed 51(27):6662–6666
39. Shukla S, Saxena S (2011) Spectroscopic investigation of confinement effects on optical properties of graphene oxide. Appl Phys Lett 98(7):073104
40. Bidram E, Sulistio A, Amini A, Fu Q, Qiao GG, Stewart A, Dunstan DE (2016) Fractionation of graphene oxide single nanosheets in water-glycerol solutions using gradient centrifugation. Carbon 103:363–371
41. Sivakumar PM, et al (2019) Polymer-graphene nanoassemblies and their applications in cancer theranostics. Anti-cancer Agents in Medicinal Chemistry

42. Luo N, Weber JK, Wang S, Luan B, Yue H, Xi X, du J, Yang Z, Wei W, Zhou R, Ma G (2017) PEGylated graphene oxide elicits strong immunological responses despite surface passivation. Nat Commun 8:14537
43. Wu Y, Ali MRK, Chen K, Fang N, el-Sayed MA (2019) Gold nanoparticles in biological optical imaging. Nano Today 24:120–140
44. Melaine F, Roupioz Y, Buhot A (2015) Gold nanoparticles surface plasmon resonance enhanced signal for the detection of small molecules on split-aptamer microarrays (small molecules detection from split-aptamers). Microarrays 4(1):41–52
45. Fantoni A, et al (2019) Plasmonic properties of gold nanospheres coupled to reduced graphene oxide for biosensing applications. In: 2019 IEEE 6th Portuguese Meeting on Bioengineering (ENBENG). IEEE
46. Liu M (2017) Plasmonic nanoparticles application in biosensor and bioimaging. Tissue Engineering And Nanotheranostics 10:151
47. Bidram E, Sulistio A, Cho HJ, Amini A, Harris T, Zarrabi A, Qiao G, Stewart A, Dunstan DE (2018) Targeted graphene oxide networks: cytotoxicity and synergy with anticancer agents. ACS Appl Mater Interfaces 10(50):43523–43532
48. Zhao P, Li N, Astruc D (2013) State of the art in gold nanoparticle synthesis. Coord Chem Rev 257(3–4):638–665
49. Binaymotlagh R, Hajareh Haghighi F, Aboutalebi F, Mirahmadi-Zare SZ, Hadadzadeh H, Nasr-Esfahani MH (2019) Selective chemotherapy and imaging of colorectal and breast cancer cells by a modified MUC-1 aptamer conjugated to a poly(ethylene glycol)-dimethacrylate coated Fe3O4–AuNCs nanocomposite. New J Chem 43(1):238–248
50. Patel AS, Juneja S, Kanaujia PK, Maurya V, Prakash GV, Chakraborti A, Bhattacharya J (2018) Gold nanoflowers as efficient hosts for SERS based sensing and bio-imaging. Nano-Structures & Nano-Objects 16:329–336
51. Jung JH et al (2010) A graphene oxide based immuno-biosensor for pathogen detection. Angew Chem 122(33):5844–5847
52. Zhang S, Xiong P, Yang X, Wang X (2011) Novel PEG functionalized graphene nanosheets: enhancement of dispersibility and thermal stability. Nanoscale 3(5):2169–2174
53. Wang C, Feng L, Yang H, Xin G, Li W, Zheng J, Tian W, Li X (2012) Graphene oxide stabilized polyethylene glycol for heat storage. Phys Chem Chem Phys 14(38):13233–13238
54. Bikhof Torbati M, Ebrahimian M, Yousefi M, Shaabanzadeh M (2017) GO-PEG as a drug nanocarrier and its antiproliferative effect on human cervical cancer cell line. Artificial cells, nanomedicine, and biotechnology 45(3):568–573
55. Li M, Wang C (2019) Preparation and characterization of GO/PEG photo-thermal conversion form-stable composite phase change materials. Renew Energy 141:1005–1012
56. Pham TA, Kumar NA, Jeong YT (2010) Covalent functionalization of graphene oxide with polyglycerol and their use as templates for anchoring magnetic nanoparticles. Synth Met 160(17–18):2028–2036
57. Jafarizad A, Taghizadehgh-Alehjougi A, Eskandani M, Hatamzadeh M, Abbasian M, Mohammad-Rezaei R, Mohammadzadeh M, Toğar B, Jaymand M (2018) PEGylated graphene oxide/Fe3O4 nanocomposite: synthesis, characterization, and evaluation of its performance as de novo drug delivery nanosystem. Biomed Mater Eng 29(2):177–190
58. Hareesh K, Williams JF, Dhole NA, Kodam KM, Bhoraskar VN, Dhole SD (2016) Bio-green synthesis of Ag–GO, Au–GO and Ag–Au–GO nanocomposites using Azadirachta indica: its application in SERS and cell viability. Materials Research Express 3(7):075010
59. Kokunov YV, Kovalev VV, Gorbunova YE, Razgonyaeva GA (2015) Supramolecular ensemble of a coordination compound of CdI 2 with 2-amino-4-methylpyrimidine. Russ J Coord Chem 41(12):787–791
60. Mello MLS, Vidal B (2012) Changes in the infrared microspectroscopic characteristics of DNA caused by cationic elements, different base richness and single-stranded form. PLoS One 7(8):e43169
61. Feng L, Li K, Shi X, Gao M, Liu J, Liu Z (2014) Smart pH-responsive nanocarriers based on nano-graphene oxide for combined chemo-and photothermal therapy overcoming drug resistance. Advanced healthcare materials 3(8):1261–1271
62. Wang X, Han Q, Yu N, Li J, Yang L, Yang R, Wang C (2015) Aptamer-conjugated graphene oxide–gold nanocomposites for targeted chemo-photothermal therapy of cancer cells. J Mater Chem B 3(19):4036–4042
63. Jibin, K., et al., Optically controlled hybrid metamaterial of plasmonic spiky gold inbuilt graphene sheets for bimodal imaging guided multimodal therapy. Biomaterials Science, 2020
64. Yang Y, Wang S, Wang C, Tian C, Shen Y, Zhu M (2019) Engineered targeted hyaluronic acid-glutathione-stabilized gold nanoclusters/graphene oxide-5-fluorouracil as a smart theranostic platform for stimulus-controlled fluorescence imaging-assisted synergetic chemo/phototherapy. Chemistry–An Asian Journal 14(9):1418–1423
65. Bahreyni A, Yazdian-Robati R, Hashemitabar S, Ramezani M, Ramezani P, Abnous K, Taghdisi SM (2017) A new chemotherapy agent-free theranostic system composed of graphene oxide nanocomplex and aptamers for treatment of cancer cells. Int J Pharm 526(1–2):391–399
66. Usman MS, Hussein MZ, Fakurazi S, Masarudin MJ, Ahmad Saad FF (2018) A bimodal theranostic nanodelivery system based on [graphene oxide-chlorogenic acid-gadolinium/gold] nanoparticles. PLoS One 13(7):e0200760
67. Pan J, Yang Y, Fang W, Liu W, le K, Xu D, Li X (2018) Fluorescent phthalocyanine–graphene conjugate with enhanced NIR absorbance for imaging and multi-modality therapy. ACS Applied Nano Materials 1(6):2785–2795
68. Azhdarzadeh M, Atyabi F, Saei AA, Varnamkhasti BS, Omidi Y, Fateh M, Ghavami M, Shanehsazzadeh S, Dinarvand R (2016) Theranostic MUC-1 aptamer targeted gold coated superparamagnetic iron oxide nanoparticles for magnetic resonance imaging and photothermal therapy of colon cancer. Colloids Surf B: Biointerfaces 143:224–232